Binding of Mg^{2+} and Ca^{2+} to Palmitic Acid and Deprotonation of the COOH Headgroup Studied by Vibrational Sum Frequency Generation Spectroscopy

Cheng Y. Tang, Zishuai Huang, and Heather C. Allen*

Department of Chemistry, The Ohio State University, 100 West 18th Avenue, Columbus, Ohio 43210, United States

Received: June 14, 2010; Revised Manuscript Received: October 13, 2010

At the air/liquid interface, cation binding specificity of alkaline earth cations, Mg^{2+} and Ca^{2+}, with the biologically relevant ligand carboxylate (COO^-) using vibrational sum frequency generation spectroscopy is reported. The empirical evidence strongly supports that the ionic binding strength is much stronger for Ca^{2+} to COO^- than that for Mg^{2+}. We conclude that at a near-neutral pH, the mechanism that governs Ca^{2+} binding to COO^- is accompanied by commensurate deprotonation of the carboxyl headgroup. In addition, surface molecular structure and ion concentration influence the cation binding behavior at the air/liquid interface. In a 0.1 M Ca^{2+}(aq) solution, Ca^{2+} initially favors forming ionic complexes in a 2:1 bridging configuration ($2Ca^{2+}$:$1COO^-$) but 1:1 chelating bidentate complexes ($1Ca^{2+}$:$1COO^-$) gradually emerge as secondary species as the system reaches equilibrium. As the Ca^{2+} concentration rises to 0.3 M, the primary complexed species exists in the 2:1 bridging configuration. Unlike Ca^{2+}, Mg^{2+} at 0.1 and 0.3 M favors a solvent-separated ionic complex with COO^-.

1. Introduction

Divalent cations are essential to the cellular physiology of living organisms. Most importantly, they play a multitude of functions ranging from assisting in protein folding, maintaining protein structures, being cofactors to the cellular nucleotides, modulating enzyme activities, and promoting signal transduction.[1] Because divalent cations such as Mg^{2+} and Ca^{2+} participate in diverse biological processes, there is considerable and sustained interest in understanding their role at a fundamental level, such as that in cellular regulatory mechanisms.[2,3] Mg^{2+} is known as an antagonist in actions of Ca^{2+} in cellular physiology; for instance, Mg^{2+} deficiency impairs Ca^{2+} metabolism. Low Mg^{2+} concentrations concomitantly raise intracellular levels of Ca^{2+}, creating an Mg^{2+}/Ca^{2+} imbalance.[2] This imbalance can cause a perpetual vasoconstriction state in smooth vascular muscle cells, a condition generally known as hypertension.[2,4]

In this article, we investigate the interaction specificity of Mg^{2+} and Ca^{2+} with biological ligands. By recognizing the unique interaction specificity of Mg^{2+} and Ca^{2+} with biological ligands, implications of their functions, selectivities, and potential binding sites in more complex systems such as transmembrane proteins can be established. Salt concentrations utilized in this study are higher than that found in mammalian blood or cytosol; however, the observation made here of concentration dependence with respect to binding complexation geometry and binding strength is clearly relevant.

To effectively investigate the cationic binding affinity with biological ligands at an interface, Langmuir monolayers and Langmuir−Blodgett (LB) films are used. Monolayers, LB films, and supported lipid bilayers (SLB) serve as proxies for the cell membrane and continue to be the prevailing model systems adopted by the surface science community.[5−7]

Previously, surface phenomena of proxy systems relating to molecular organization,[8] surface aggregation,[9] film morphology,[10] and molecular interactions[11] have been explored. Surface techniques have been applied to these research areas. Among them, Langmuir trough instruments have been traditionally used for surface pressure−area ($\pi-A$) isotherms to reveal macroscopic phase behavior of surface films.[12] Brewster angle microscopy and fluorescence microscopy have been widely applied in studies of film morphology of Langmuir monolayers at aqueous surfaces;[13,14] likewise, atomic force microscopy and scanning electron microscopy are candidates of choice for LB films on solid substrates.[15,16] X-ray diffraction and neutron scattering techniques have also become more frequently employed in studies of surface molecular structures and phase behavior of surface films in crystalline states at both aqueous and solid surfaces.[17,18] Infrared reflection absorption spectroscopy (IRRAS) is capable of providing molecular structure information of surface molecules.[19] However, not all techniques described here are applicable to surfaces in direct contact with liquids or vapors. For instance, gas phase interference complicates data processing in important spectral regions using infrared based techniques. In practice, complex normalization and background subtraction are commonly performed to achieve quality spectra. In the work presented here, vibrational sum frequency generation (VSFG) spectroscopy is used because it is interface-selective and, therefore, provides vibrational information only from the interfacial molecules. Although VSFG utilizes infrared in addition to visible light, it is relatively insensitive to vapor phase absorbers, since the upconversion of the infrared with visible light takes place only at the interface due to the lack of inversion spectroscopic selection rule.

It has been observed that the presence of certain cations in aqueous solution promotes LB film transfer efficiency and film integrity; for instance, empirical evidence suggests that Cd^{2+} and Pb^{2+} have these characteristics because of their strong binding affinities.[19] To gain more insight into ionic binding behavior of various divalent cations, ranging from alkaline earth metals, transition metals, and main-group metals to long-chain fatty acids at the air/aqueous interface, Hühnerfuss and coworkers determined the possible binding configurations of the coordination complexes produced.[20,21] They further evaluated the competition behavior of the metal cations with hydronium

* Corresponding author. E-mail: allen@chemistry.ohio-state.edu.

10.1021/jp105472e
Published on Web 11/09/2010

ions in increasingly acidic environments. Later, more studies of similar systems were conducted by other groups.[22−25] These studies incorporated more metal cation species and different surfactant molecules, yet the binding behavior of alkaline earth cations is still not well understood.

Alkaline earth cations have a weaker binding affinity to the carboxylate (COO^-) group relative to transition metal and main-group metal cations. Due to their noble-gas electron configuration, both Mg^{2+} and Ca^{2+} interactions were considered by some researchers to be purely ionic in nature when interacting with negatively charged ligands such as COO^-; in other words, this kind of interaction was thought to be nonspecific.[3,26,27] On the contrary, a covalent type of interaction of Mg^{2+} and Ca^{2+} with COO^- was suggested in other studies.[20,23] For instance, a 1:1 bidentate coordination complex of Ca^{2+}/COO^- has been proposed by Liu and co-workers.[28] Furthermore, Dutta and co-workers concluded that Mg^{2+} could interact so strongly with COO^- in the heneicosanoic acid (C_{22}, HA) monolayer at the air−aqueous interface that it promoted formation of a superlattice structure in the monolayer film, similar to the outcome induced by Cd^{2+} and Pb^{2+}.[29] These disparate views indicate that further studies are necessary to elucidate the intermolecular and interionic interactions, and therefore, VSFG, a highly sensitive second-order optical spectroscopy, is utilized in the work presented here.

Second-order nonlinear optical techniques are deemed powerful in studying surface phenomena that are physicochemical in nature by providing surface specificity and molecular moiety sensitivity. For instance, Geiger and co-workers used the second harmonic generation technique to evaluate adsorption phenomena of the carboxylic acid functionalized fused silica/water interface in the presence of divalent cations and asserted that the studied cations, including Ca^{2+}, deprotonate the carboxylic acid head groups.[30] Richmond and co-workers applied VSFG to study adsorption of carboxylate anions at the CaF_2/water interface.[31] As a second-order nonlinear optical technique, VSFG responds only to media that possess lack of inversion symmetry; therefore, any contribution from isotropic media or bulk is disallowed. In this regard, surfaces or interfaces between two isotropic media are active toward sum frequency generation. Furthermore, resonant enhancement of the SFG intensity is realized by tuning the laser frequency to match the vibrational transitions of the interfacial molecules. IRRAS is sensitive to Langmuir monolayers if sufficient scans are taken to obtain spectra with good signal-to-noise ratios; however, this technique is not surface-selective, considering its probe depth being proportional to its wavelength. Hence, signal contribution from bulk is significant for IRRAS. In addition, VSFG is a coherent process in which laser pulses provide large numbers of photons, and the VSFG intensity is proportional to the square of the interfacial number density of oscillators, whereas IRRAS scales linearly with absorbers.

In this study, VSFG is applied to systematically investigate the ionic binding specificity of biologically relevant cations Mg^{2+} and Ca^{2+} to a palmitic acid (C_{16}, PA) monolayer at air/aqueous interfaces. The vibrational modes investigated encompass both head and tail groups of the PA molecules. The νCO/δOH, $\nu_s COO^-$, νC═O, and νCH of PA were probed. Of primary importance is the identification of the ionic binding specificity of Ca^{2+} to COO^- relative to Mg^{2+}.

2. Experimental Section

2.1. Materials. Palmitic acid (>99%, Sigma-Aldrich) and acyl chain deuterated palmitic acid (>98%, Cambridge Isotope Laboratories, Inc.) were used to prepare solutions at ∼1.5 mM by dissolving in spectroscopic-grade chloroform (>99.9, Sigma-Aldrich). Magnesium chloride hexahydrate (certified ACS, 99%, Fisher Scientific) and calcium chloride dihydrate (USP/FCC, 99%, Fisher Scientific) were used to prepare stock solutions by dissolving in deionized (ultra pure) water with 18.2 MΩ cm resistivity from a Barnstead Nanopure system at pH of 6.0.

Stock solutions were filtered twice to eliminate potential organic contaminants using a Whatman Carbon-Cap activated carbon filter. The concentrations of the filtered stock solutions were standardized on the basis of the Mohr titration technique in which silver nitrate (reagent grade, Fisher Scientific) and potassium chromate (99.5%, E.M. Science) were used as a titrant and an indicator, respectively.[32] Serial dilution was used to prepare 0.1 and 0.3 M inorganic salt solutions. Note that all experiments were conducted at neutral pH (water not purged of carbon dioxide, pH of 6), except for the pH control experiment. In the pH control experiment, solutions with varied pH values were prepared by gradually mixing an appropriate amount of concentrated HCl (37%, reagent grade, Fisher Scientific) or NaOH (99%, reagent grade, Fisher Scientific) stock solution (0.2 M) in ultrapure water. To ensure obtaining accurate pH values of solutions used in the experiment, each individual solution was uniformly stirred after serial additions of concentrated acid or base solutions to 250 mL of ultra pure water. Once the pH meter (Accumet Basic AB15, Fisher Scientific) reading was close to the desired value, 20 min time was allowed for equilibration under ambient conditions, and the final pH reading was recorded. (In the pH study, addition of the HCl and NaOH is assumed that the ions used to achieve the change in pH do not to bind to the headgroup.) In addition, all prepared solutions were sealed and conditioned at room temperature (23 ± 1 °C) for over 24 h before use.

2.2. Methods. ***2.2.1. Langmuir Film Balance.*** A KSV minitrough (KSV, Finland), 176.5 mm × 85 mm, was used to acquire surface pressure−area (π−A) isotherms. The trough and the two barriers are made of Teflon and Delrin, respectively. During compression, the π−A isotherms were recorded in real time by the Wilhelmy plate method.[33] The subphase temperature was maintained at 23 °C after 24 h equilibration in a climate-controlled room (23 °C). All π−A isotherms were collected in a Plexiglas box to eliminate any possible contaminant. The aqueous surface was compressed and examined for any sign of surface pressure increase to ensure negligible organic contamination prior to spreading the PA Langmuir monolayer. After confirming the surface purity, tens of microliters of PA-chloroform solution were spread in a dropwise fashion by a microsyringe (Hamilton) for homogeneous spreading. Ten minutes was allowed for complete solvent evaporation. During compression, a constant rate of 5 mm/min of both barriers was employed. In SFG experiments that probe vibrational information of the monolayers at different surface pressures, the minitrough was placed on a height-adjustable sample stage to allow incidence of the two-incident laser beams. Next, the same monolayer spreading protocol was followed to prepare the PA Langmuir monolayers. VSFG spectra were taken while monolayers were maintained at the predetermined surface pressures.

2.2.2. Monolayer at Equilibrium Spreading Pressure. Monolayers at equilibrium spreading pressure (ESP) were spread over inorganic salt solutions in Petri dishes. The monolayers of PA at ESP are known to be highly ordered. After spreading, 10 min time was also allowed for solvent evaporation and monolayer stabilization, then VSFG spectra were acquired. In time-evolution studies, VSFG spectra were taken in a sequential

manner with 5 min acquisition time until systems reached equilibrium after 60 min, evidenced by constant spectral intensities. To ensure the same overlap throughout the spectral acquisition, VSFG signal incident on the CCD camera was maintained on the same pixel rows by adjusting the sample stage height to compensate for the potential evaporation loss.

2.2.3. Brewster Angle Microscopy. The Langmuir trough was used in a morphology study of surface monolayers using an in-house Brewster angle microscope (BAM). The setup is enclosed in a black Plexiglas housing. The trough is situated on a sample stage located in the middle of two optomechanical arms of a goniometer that provides both height and angle adjustments. A collimated laser beam from a He:Ne diode module (Research Electro Optics, Inc.) with polarization ratio of 500:1 is incident onto the air/water interface at the Brewster angle (53°). First, a Glan−Thompson polarizer is used to purify the p-polarized light incident on the sample. The reflected beam is collected by an industrial Nikon 20× objective mounted on the detection arm, and then via a tube lens directed onto a CCD camera (Andor, 512 × 512 pixels, DV412). No additional image processing was implemented. On average, the BAM images acquired have resolution better than 10 μm, sufficient for observing film domains at air/aqueous interfaces.

2.2.4. Vibrational Sum Frequency Generation Spectrometer. The broad bandwidth VSFG spectrometer setup has been described elsewhere.[34−36] A titanium:sapphire oscillator (Spectra-Physics, Tsunami) with an optimal center wavelength at 785 nm and a sub-50 fs (fs) pulse width seeds two 1-kHz regenerative amplifiers (Spectra- Physics, Spitfire, femtosecond and picosecond (ps) versions) that are pumped by a solid state Nd:YLF laser (Spectra-Physics, Evolution 30) at 527 nm. The resulting laser beams from the two respective regenerative amplifiers are 85 fs pulses at 785 nm (22 nm bandwidth) and 2 ps pulses at 785 nm (17 cm^{-1} bandwidth). In an optical parametric amplifier (Light Conversion, TOPAS), the amplified femtosecond laser pulses from the femtosecond regenerative amplifier are used to generate amplified parametric waves (signal and idler) via a BBO crystal using three general steps: superfluorescence generation, preamplification, and power amplification of the signal beam. The amplified signal and idler beams are then used to create an infrared beam via an $AgGaS_2$ crystal in the nonlinear difference-frequency generation system (Light Conversion, NDFG connected to the TOPAS). On average, the spectral bandwidth (fwhm) of the resultant broadband infrared beam is 200 cm^{-1} in the spectral regions under investigation, and because it is a broadband infrared pulse, good signal-to-noise-ratio VSFG spectra are acquired for durations ranging from 30 to 300 s, depending on the cross sections of the vibrational modes of interest. The output of the infrared beam can easily cover from 1000 to 4000 cm^{-1} with strong energy outputs, as predicted by tuning curves for BBO (type II phase matching) and $AgGaS_2$ (type I phase matching) crystals and the crystal nonlinear conversion efficiencies. For instance, the average infrared energies at the sample stage in this study were measured to be 8, 9, and 14 μJ in spectral regions of νCO/δOH and $\nu_s COO^-$ (1250−1550 cm^{-1}), νC═O (1600−1800 cm^{-1}), and νC−H (2800−3000 cm^{-1}), respectively. Furthermore, to minimize an energy loss of the infrared beam and an overwhelming spectral interference from water vapor absorption, 95% of the infrared beam path was purged with dry nitrogen gas (in-house). In addition, 300 μJ visible energy was utilized for VSFG in this study.

As stated above, the probe beams consisting of the 785 nm visible beam and the broadband infrared beam need to overlap at the sample surface spatially and temporally for the SFG process. The incident angles of visible and infrared beams are 53° and 70°, respectively. The generated VSFG signal from the sample surface is detected in reflection. The signal is first dispersed by a monochromator (Acton Research, SpectraPro SP-500 monochromator with a 1200 g/mm grating blazed at 750 nm) and then is detected by a liquid-nitrogen-cooled CCD camera (Roper Scientific, 1340 × 400 pixel array, LN400EB back illuminated CCD). During this study, the polarization combination used was ssp (s-SFG; s-visible; p-infrared). To arrive at the final VSFG spectra, background-subtracted VSFG spectra were normalized against the broadband infrared beam energy profile using a nonresonant VSFG spectrum from a GaAs crystal (Lambda Precision Optics, Inc.). The purpose of doing the normalization is to eliminate the spectral distortion caused by the infrared beam energy distribution associated with each frequency in the spectral region of interest. In addition, spectra were fitted on the basis of Lorentzian lineshapes using a routine with global constraints developed in our laboratory. Spectral calibration of VSFG peak positions was completed by comparing the polystyrene absorption bands obtained from a nonresonant GaAs spectrum with reference FTIR spectra. By doing this, the VSFG peak positions reported here are accurate to 1 cm^{-1}.

3. Results and Discussion

3.1. Palmitic Acid: Brewster Angle Microscopy and Compression Isotherms. $\pi-A$ isotherms of Langmuir monolayers on aqueous surfaces are frequently used to reveal the underlying phase information of the monolayer being subject to constant compression. The macroscopic phase behavior using the isotherms of PA monolayers on aqueous alkaline earth solutions were investigated and are shown in Figure 1, along with Brewster angle images of the pure PA surface to confirm the phase assignments. Figure 1B and C show the $\pi-A$ isotherms of PA monolayers on aqueous Mg^{2+} and Ca^{2+} solutions at 0.1 and 0.3 M, respectively. To facilitate a direct comparison, the isotherm on neat water is shown in these plots. Being saturated single acyl chains, PA molecules are fairly compressible, and ultimately, can be packed in a highly ordered structure at high surface pressures. The isotherm of the PA monolayer on neat water reveals this behavior. In the order of decreasing mean molecular area (MMA), the PA monolayer undergoes multiple phase transitions that include the gas and tilted condensed (G-TC) coexistence phase to the tilted condensed (TC) phase followed by the TC to the untilted condensed (UC) phase, then it collapses.

Brewster angle microscopy images of the PA monolayer on neat water are shown as insets to Figure 1A. The image obtained at a MMA of 46 $Å^2$/molecule reveals the existence of domains, which indicates two-dimensional condensing of the monolayer and, thus, the assignment of a coexistence region of a TC phase with the G phase. Another image of the monolayer was obtained just after the G-TC-to-TC transition. This image reveals a homogeneous film consistent with the TC phase assignment. The transition from the TC phase to the UC phase corresponds to a second-order phase transition.[17] Similar to other fatty acid homologues, the PA monolayer shows finite surface pressure at a relatively small MMA of 21 $Å^2$/molecule, which is typical for monolayers of saturated fatty acids.[37] In addition, the second-order phase transition occurs at 24 mN/m, with a corresponding MMA of 17 $Å^2$/molecule, and the collapse pressure occurs at 50 mN/m, consistent with previous studies.[26]

In the presence of Mg^{2+} cations, some deviations are found in comparison with the isotherm obtained from the neat water

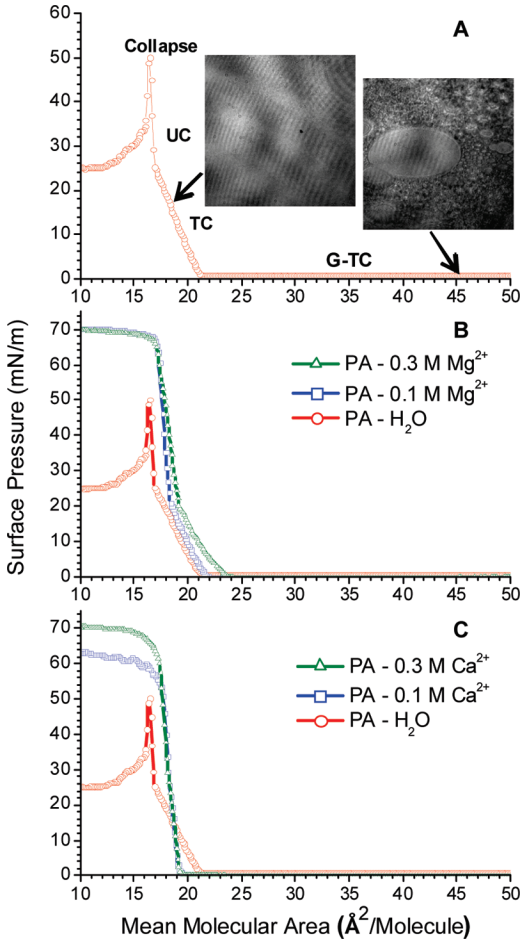

Figure 1. Surface pressure−area isotherms (π−A) of PA monolayer at 23 °C on aqueous surfaces, neutral pH: (A) neat water with, on the right, Brewster angle microscopy images in the G-TC coexistence region and, on the left, the TC homogeneous phase region; (B) neat water and $MgCl_2$ (0.1 and 0.3 M); and (C) neat water and $CaCl_2$ (0.1 and 0.3 M).

surface. Figure 1B shows that the PA monolayers collapse at a much higher surface pressure at 70 mN/m on 0.1 and 0.3 M Mg^{2+}(aq) solutions. This kind of behavior is caused by an increase in the surface tension in inorganic salt solutions.[33] The second-order phase transition occurs at a lower surface pressure on Mg^{2+}(aq) solutions than on neat water. This trend has also been observed in the PA monolayers on aqueous alkali solutions.[36] Clearly, each PA molecule in the monolayers occupies a slightly larger MMA on the Mg^{2+}(aq) solution in the UC phase. The average MMA is 17 Å^2/molecule on neat water, as opposed to 19 Å^2/molecule on the Mg^{2+}(aq) solutions. To explain the observed discrepancy, cationic interactions with headgroups in the form of charge screening have been suggested.[26] Nevertheless, it is evident that at the same surface pressure, the PA monolayers on the Mg^{2+}(aq) solutions undergo less compression than on neat water. Because the surface pressure directly correlates with the van der Waals interaction between adjacent acyl chains, an orderly packed structure can maximize interactions with an all-trans conformation.[38] Therefore, the presence of Mg^{2+} at 0.1 and 0.3 M could induce the PA monolayers to be in the all-trans conformation at MMA of 19 Å^2/molecule. In addition, the corresponding shift on the MMA in the TC phase could be explained by the electrostatic repulsion between neighboring charged species as a result of deprotonation, as confirmed by VSFG results and discussed later.

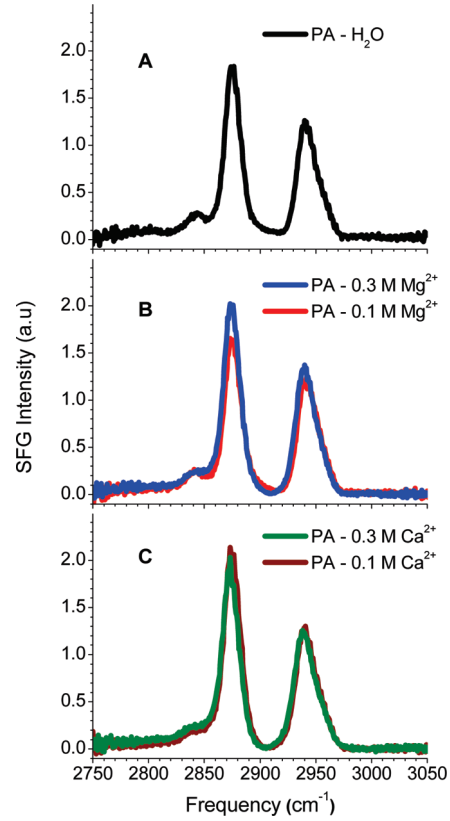

Figure 2. ssp VSFG spectra in the CH stretch region of PA monolayers on aqueous solutions at 10 mN/m, neutral pH: (A) neat water, (B) 0.1 and 0.3 M $MgCl_2$, and (C) 0.1 and 0.3 M $CaCl_2$.

Figure 1C shows the π−A isotherms of the PA monolayers on the Ca^{2+}(aq) solutions at 0.1 and 0.3 M, respectively. The π−A isotherms acquired from the monolayers on Ca^{2+} (aq) solutions are different from that from neat water and the Mg^{2+}(aq) solutions: First, the TC phase disappears, as well as the second-order phase transition. Second, the PA monolayers directly transition from the coexistence phase to the UC phase and then collapse. This behavior has been attributed to the condensing effect of metal cations as a result of forming fatty acid salts.[39] In the UC phase, the PA monolayers are similar between the Ca^{2+}(aq) solutions and Mg^{2+}(aq) solutions. The disappearance of the TC phase is further explored below.

3.2. VSFG Spectroscopic Data of PA Monolayers. A molecular-level understanding is the prerequisite to decipher the observed disparity between the π−A isotherms on the aqueous Mg^{2+} and Ca^{2+} solutions. To gain insight, VSFG spectra were obtained from four spectral regions: the stretching vibrations (ν) of C−H at 2800−3000 cm^{-1}, the C−O (mixed with the bending mode of OH) at 1200−1400 cm^{-1}, the COO^- at 1400−1500 cm^{-1}, and the C═O at 1700−1800 cm^{-1}.

3.2.1. C−H Stretching Region (2800 − 3000 cm^{-1}). VSFG spectra in the C−H stretching region directly reveal the conformational order of the acyl chains in the PA monolayers by analyzing the relative intensity of the CH_3 and the CH_2 peaks.[8] By selectively controlling the surface pressure, structural information of the PA monolayers in each distinct phase can be interrogated and compared. Figure 2A, 2B, and 2C show the ssp VSFG spectra of the PA monolayers on the neat water surface, the Mg^{2+}(aq) solutions, and the Ca^{2+}(aq) solutions (0.1 and 0.3 M) surfaces at 10 mN/m. Four vibrational modes are assigned: the methylene symmetric stretch (ν_sCH_2) at 2842 cm^{-1}, the methyl symmetric stretch (ν_sCH_3) at 2874 cm^{-1}, and in the larger asymmetrically shaped peak at higher frequency consist-

ing of the methyl Fermi resonance ($\nu_{FR}CH_3$) at 2940 cm^{-1} and the methyl asymmetric stretch (ν_aCH_3) at 2960 cm^{-1}. Among them, the ν_sCH_3 and the $\nu_{FR}CH_3$ peaks are strong, whereas the ν_sCH_2 and the ν_aCH_3 peaks remain relatively weak as lower and higher frequency shoulders, respectively. There are only small differences observed between each spectrum.

In Figure 2A, the ν_sCH_2 peak is much weaker than the ν_sCH_3. This observation is indicative of the conformational ordering of the acyl chains at 10 mN/m. On the basis of the electric dipole approximation, SFG is not active in a centrosymmetric environment.[40] Therefore, a weak ν_sCH_2 peak accompanied by a strong ν_sCH_3 peak reflects the formation of centrosymmetry between adjacent CH_2 groups when the acyl chains are near the all-trans conformation. Compared with the spectrum on the water surface, the PA spectrum on the 0.1 M Mg^{2+}(aq) solution (Figure 2B) is similar. But on the 0.3 M Mg^{2+}(aq) solution, the ν_sCH_3 peak is slightly stronger, and concomitantly, the ν_sCH_2 peak becomes slightly weaker relative to those on the 0.1 M. (Although the y axis is in arbitrary units, the scales can be compared.) These intensity changes suggest that the acyl chain of PA is more ordered when the Mg^{2+}(aq) solution concentration is increased from 0.1 to 0.3 M at the same surface pressure. However, this trend is not followed on the Ca^{2+}(aq) solutions, as evidenced in Figure 2C. For instance, both ν_sCH_2 and ν_sCH_3 peak intensities remain constant, irrespective of the concentration increase, and the overall peak intensity and the spectral shape match those on the 0.3 M Mg^{2+}(aq) solution, revealing more order; that is, minimal contribution from gauche defects.

As shown in the $\pi-A$ isotherms, Ca^{2+} demonstrates the condensing effect on the acyl chains, which consequently leads to the absence of the TC phase. Similarly, the respective VSFG spectra on the Ca^{2+}(aq) solutions consistently affirm this effect, depicting a larger intensity ratio of the ν_sCH_3 over the ν_sCH_2 than the ratio on the neat water surface at 10 mN/m. Qualitatively, the larger the ratio, the more ordered the acyl chains, revealing near-all-trans conformation. In comparison, the structural ordering of the PA monolayers on the Mg^{2+}(aq) solutions and Ca^{2+}(aq) solutions is similar at 0.3 M in the TC phase, but not at 0.1 M. Hence, Mg^{2+} at a lower concentration (0.1 M) is less effective in interacting with the PA molecules, as compared with Ca^{2+}. In other words, a condensing effect is much more pronounced in Ca^{2+} than in Mg^{2+}. This was also indicated from previous IR studies from monolayer films that were removed (skimmed) from aqueous divalent salt solution surfaces.[41] Unlike the spectral features demonstrated in the spectra obtained at 10 mN/m, the overall spectral intensity and shape becomes indistinguishable when the PA monolayers are in the UC phase, surface pressures above 24 mN/m for the aqueous Mg^{2+} subphases, but above 0 mN/m for the Ca^{2+} (Supporting Information). This result implies that in the UC phase, the degree of conformational ordering is similar, irrespective of the subphase. This observation agrees with the high compressibility of PA monolayers at the air/aqueous interface. To summarize, the spectral variations are small in the C−H stretching region. Therefore, direct evidence revealing cation binding behavior to the headgroups is imperative in clarifying the isotherm differences.

3.2.2. Carboxyl and Carboxylate Symmetric Stretching Region (1300 − 1500 cm^{-1}). The contribution from the C−H scissoring mode around 1400 cm^{-1} is significant enough to complicate the spectral signatures from the PA headgroup in this spectral region. Thus, isotopic labeling was used to eliminate the spectral interference. Hence, PA molecules with perdeuterated acyl chains (D_{31}-PA) were used for VSFG studies in this spectral region.

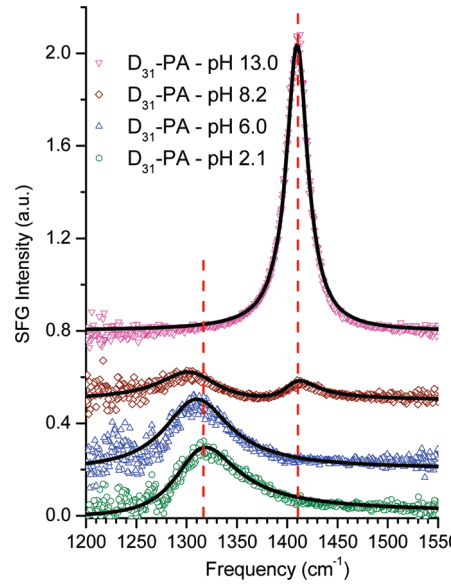

Figure 3. ssp VSFG spectra in the COO^- stretch region of D_{31}-PA monolayers on water with pH values of 2.1, 6.0, 8.2, and 13.0. Fitted curves are shown as solid lines. Spectra are offset for clarity.

3.2.2.1. pH Control Study. To accurately assign the ν_sCOO^- peak in the spectral region around 1400 cm^{-1}, a control experiment was first performed by selectively adjusting the pH in the bulk. Figure 3 shows the ssp VSFG spectra of the D_{31}-PA monolayers spread on aqueous surfaces at pH 2.1, 6.0, 8.2, and 13.0, respectively, at the equilibrium spreading pressure (ESP) of D_{31}-PA. A relatively small intensity peak at 1300 cm^{-1} is present with almost equal strength as the pH 2.1 and 6.0 solutions, whereas an intense and symmetric peak at 1410 cm^{-1} appears with the pH 13.0 solution. At pH 8.2, both peaks are observed. According to the literature, the 1300 cm^{-1} peak is assigned to the C−O stretch of the protonated carboxyl group.[25] This peak has been observed previously in a VSFG study of interfacial acetic acid solutions and IRRAS studies on fatty acid monolayer systems.[25,42] The 1410 cm^{-1} peak is commonly ascribed to the ionic or hydrated form of COO^- in aqueous solution; in addition, this peak has also been identified by Miranda et al. on hexacosanoic acid (C_{26})-film-covered surface at pH 12.0 using VSFG.[43] The pK_a value of the carboxylic acid group is ∼4.85 in the bulk, but it rises to ∼8.7 for long-chain fatty acids at the air−liquid interface.[44,45] Therefore, our result is consistent with the fact that the D_{31}-PA in the monolayers are protonated at pH of 6 and below, yet are fully deprotonated when the pH reaches 13.0; and moreover, at pH 8.2, we observe both protonated and deprotonated species consistent with the surface pK_a. In summary, this empirical evidence strongly suggests that the surface pK_a's of long-chain fatty acids are significantly greater than the measured value in the bulk. By varying the aqueous pH conditions, the respective spectra affirm the underlying acid−base chemistry of the D_{31}-PA Langmuir monolayer at the air/liquid interface. Although the ionic strength of solution influences electrical interactions in general, the addition of concentrated HCl or NaOH solution to ultrapure water is small enough to affect only the headgroup charge state, not the electrical interaction between the neutral headgroup and the dissolved ions.

3.2.2.2. Mg^{2+} vs Ca^{2+}. Next, a direct interrogation of the underlying binding behavior of Mg^{2+} and Ca^{2+} to the D_{31}-PA headgroup was undertaken. Figure 4A and B show, respectively, the ssp spectra of D_{31}-PA monolayers on the Mg^{2+}(aq) solutions and Ca^{2+}(aq) solutions at 0.1 and 0.3 M and at a neutral pH.

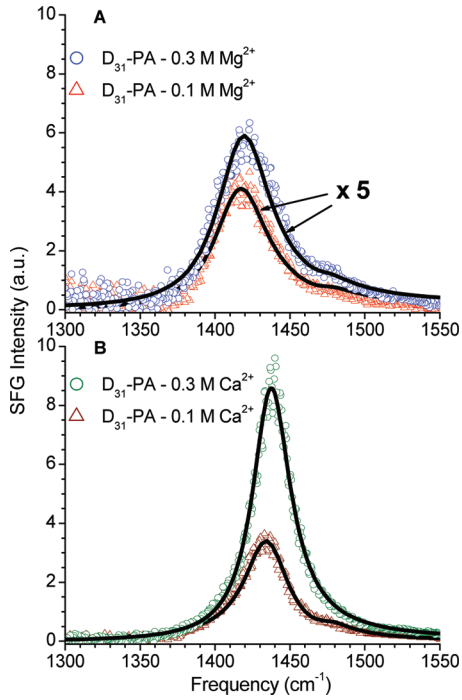

Figure 4. ssp VSFG spectra in the COO^- stretch region of D_{31}-PA monolayers on salt solutions at near neutral pH: (A) 0.1 and 0.3 M $MgCl_2$ and (B) 0.1 and 0.3 M $CaCl_2$ solutions. The individual fitted curves are shown as solid lines. The peak intensities in Figure A are enhanced 5 times for comparison purposes.

By direct observation, the spectra of Figure 4A (magnified 5 times for clarity) reveals two resonances: a dominant peak centered at 1417 cm^{-1} and a weak shoulder centered at 1475 cm^{-1}. In addition, there is a slight increase in the peak intensities when the concentration is increased from 0.1 to 0.3 M. In contrast, the spectral features shown in Figure 4B are very different, bearing only a small resemblance to the spectra collected from the aqueous Mg^{2+} solutions. One intense, symmetric peak positioned at 1435 cm^{-1} is observed from the 0.3 M Ca^{2+} solution, whereas a similar, but less intense, peak is seen at the same spectral position from the 0.1 M Ca^{2+} solution; however, in the 0.1 M spectrum, a small shoulder at 1475 cm^{-1} similar to the 0.1 M Mg^{2+} solution is also evident. In evaluating the spectral differences exhibited in Figure 4A and B, not only are different peak positions found, but the overall intensity is significantly enhanced with the Ca^{2+} subphase compared with that of the Mg^{2+} subphase.

Because of the complete isotopic substitutions of the acyl chain, there is not a CH_2 scissoring mode contribution in the spectra of Figure 4. Hence, the observed peaks at three distinct spectral positions are assigned here solely to the COO^- in three different chemical environments or three different COO^- complexes. Blue shifting of the dominant peak from 1417 to 1435 cm^{-1} coincides with the degree of deprotonation. The spectral evidence reveals a stark contrast between the degrees of deprotonation on the carboxylic headgroup induced by Mg^{2+} versus Ca^{2+}. On the basis of the spectral intensity alone, Ca^{2+} clearly induces greater degrees of deprotonation than Mg^{2+}. We confirm this by additional spectral evidence, as discussed below.

The 1417 cm^{-1} peak from the Mg^{2+}(aq) solutions (Figure 4A) resemble the 1410 cm^{-1} peak as shown on the pH 13.0 aqueous solution in terms of the peak position; therefore, we assign the former to the hydrated species of COO^- as previously stated. Very importantly, a similar peak has also been observed from D_{31}-PA monolayers on aqueous Na^+ and K^+ solutions,[36] with spectral features similar between the Na^+ from that study and the Mg^{2+}subphase studied here. Because both Na^+ and Mg^{2+} favor full hydration, a solvent barrier is likely present during ionic interactions between the ion and the headgroup. Despite this, the peak occurs at 1414 cm^{-1} on alkali salt solutions. Similar spectral broadening also takes place on the aqueous Mg^{2+} solution due to a population broadening when the deprontonated and protonated D_{31}-PA molecules coexist at the interface.[23] Furthermore, the surface charge density of Mg^{2+} is much higher than Na^+, which then implies that Mg^{2+} tends to possess a much stronger hydration shell than that of Na^+ and behaves predominantly as a hydrated entity in the bulk, which minimizes any direct ionic interaction or formation of ionic complex with COO^-. According to Figure 4A, Mg^{2+} behaves much like a hydrated entity when it binds to the headgroup. Nevertheless, the peak at 1475 cm^{-1} is also present in the spectra, indicating the existence of other possible COO^- species. On the basis of conclusive evidence obtained from a similar study of the D_{31}-PA monolayers on K^+ solutions, the 1475 cm^{-1} peak was assigned to the 1:1 ionic complex of K^+/COO^- that exists in a greater proportion on 0.6 M K^+(aq) solution.[36] Therefore, the small shoulder positioned at 1475 cm^{-1} is accordingly attributed to the 1:1 ionic complex of Mg^{2+}, COO^- and counts for only ~5% of the total COO^- population. Hence, on aqueous Mg^{2+}, the predominant species of COO^- in the D_{31}-PA monolayers exists as a hydrated species accompanied by a smaller fraction of the 1:1 ionic complex.

In contrast to the spectra shown in Figure 4A, the ssp VSFG spectra of D_{31}-PA on the Ca^{2+}(aq) solutions are starkly different (Figure 4B). The single intense peak at 1435 cm^{-1} on the 0.3 M Ca^{2+}(aq) solution is ~8 times stronger than the corresponding spectrum on the 0.3 M Mg^{2+}(aq) solution. Even though spectral peaks in close proximity to 1435 cm^{-1} sparsely appear in IRRAS spectra collected from similar systems at the air/liquid interface, no in-depth elaboration has been given regarding these peaks due to weak signals.[25] According to infrared selection rules, the asymmetric carboxylate stretching ($\nu_a COO^-$) peak is inherently stronger than the $\nu_s COO^-$ peak, as evidenced in IRRAS spectra.[20,21] Thus, most spectral analyses focused on the $\nu_a COO^-$ and δCH_2 peaks in obtaining molecular structural information, but because the $\nu_a COO^-$ was not detected using VSFG, no direct comparison can be made between them.

It is commonly accepted that Ca^{2+} favors binding to oxygen atoms, especially in biologically relevant ligands such as carboxylate, carbonate, and phosphate groups, to form insoluble complexes that play critical roles in biological processes.[46] For instance, postulates such as matching ionic size, dynamic hydration shell, and ion−water affinity between Ca^{2+} and COO^- have been given to explain their strong binding affinities. However, the true nature of how Ca^{2+} interacts with COO^- continues to remain as a puzzle without further support of concrete experimental evidence. In IRRAS studies, the difference in the spectral peak positions between the $\nu_a COO^-$ and $\nu_s COO^-$, or the so-called Δ value, has been regularly employed to determine the possible coordination type between the metal cations and the headgroup.[47−50] So far, four types of complex species have been determined: ionic complex, monodentate complex, chelating bidentate complex, and bridging complex.[51] Because Ca^{2+} has a low Pauling electronegativity and a complete electronic valence shell, Ca^{2+} is thought to bind mostly as an ion with COO^-, although this binding may possess some covalent binding character.[20]

According to Figure 4B, the intensity ratio of $\nu_s COO^-$, 0.3 M to $\nu_s COO^-$, 0.1 M is close to 2.1. Because the VSFG signal

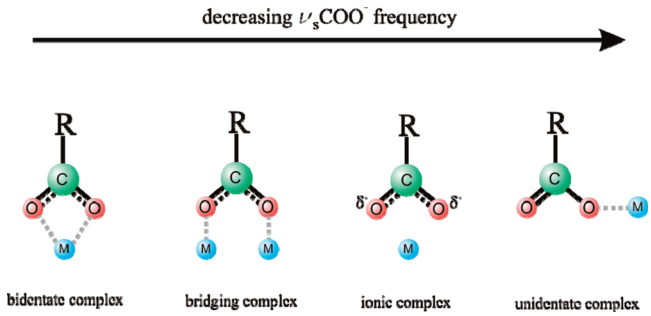

Figure 5. Pictorial illustrations of four possible metal−carboxylate complexes in the order of decreasing $\nu_s COO^-$ frequency. R represents an alkyl chain.

intensity is proportional to the molecular number density square (N^2) for an all-trans configuration, by taking the square root of this ratio, the ratio in terms of the number density of COO^- is then close to 1.5, assuming no orientation change of the COO^- at both concentrations and insignificant nonresonant contributions. On the other hand, the corresponding concentration ratio of the Ca^{2+}(aq) solution is 3; therefore, the ratio between the number of Ca^{2+} per COO^- or per one deprotonation event is 2:1, indicating a 2:1 (Ca^{2+}/COO^-) bridging ionic complex, as opposed to the 1:1 bidentate ionic complex that exists between K^+ and COO^- as shown in the previous study.[36] Although this kind of ionic ratio has never been identified for Ca^{2+}, in the high concentration Ca^{2+}(aq) solution as used in this study, this type of ionic complex is dominant. By adopting this type of ionic complex geometry, the condensing effect observed in the $\pi-A$ isotherms appears to be consistent with the bridging configuration. In addition, the Δ value (difference between the ν_s and the ν_a) analysis also supports our assignments. From previous studies,[52] the hydrated ionic complex has a Δ value of 168 cm^{-1}, with the $\nu_s COO^-$ at 1410 cm^{-1}, whereas this value tends to be much smaller in the 1:1 bidentate complex and slightly smaller in the 2:1 bridging complex. Hence, in evaluating the $\nu_s COO^-$ mode in this study (we do not observe the ν_a), the 1475 and 1435 cm^{-1} peaks consistently follow this convention in terms of coordination configurations. Figure 5 illustrates these configurations and their associated frequencies, as observed here.

To ensure that the D_{31}-PA monolayers exist as stable monolayers on both Mg^{2+}(aq) solutions and Ca^{2+}(aq) solutions (0.1 and 0.3 M), a time evolution study of the $\nu_s COO^-$ was carried out. Among all, only spectra acquired from the 0.1 M Ca^{2+}(aq) solution exhibit a dynamic nature of the peak evolution, whereas spectra from other solutions remain almost unchanged during the time of spectral acquisition. Figure 6 shows the ssp VSFG spectra of D_{31}-PA on 0.1 M Ca^{2+}(aq) solution at four times with respect to the initial time zero set to be after 10 min following spreading of monolayers (to allow solvent evaporation) with integration times of 5 min. The trend shows that the 1435 cm^{-1} peak intensity gradually decreases, while the 1475 cm^{-1} peak evolves into shape. After 60 min, the overall spectral intensity becomes constant as the system reaches equilibrium.

On the contrary, Figure 7 shows the ssp spectra of the D_{31}-PA monolayer on the 0.3 M Ca^{2+}(aq) solution where the 1435 cm^{-1} spectral intensity decreases somewhat with time as a result of film relaxation, but the 1475 cm^{-1} shoulder stays relatively constant throughout the time of spectral acquisition. These results show the dynamic nature of the ionic complex species that exists on the aqueous Ca^{2+} solutions. As previously stated, the 1435 cm^{-1} peak is assigned to the 2:1 bridging ionic complex, and the 1475 cm^{-1} peak, to the 1:1 bidentate ionic complex. According to the spectra in Figures 6 and 7, the 2:1 bridging ionic complex exists as the sole species for the 0.3 M Ca^{2+} subphase, irrespective of allowing sufficient time for possible structural rearrangement; however, at 0.1 M Ca^{2+}, the 2:1 bridging complex is predominant from the beginning, although contribution from the 1:1 bidentate ionic complex gradually emerges as a secondary species as time elapses.

To elucidate this markedly different behavior exhibited by Ca^{2+}, it is important to realize that on the 0.3 M Ca^{2+} subphase, the majority of D_{31}-PA molecules are deprotonated. Complete deprotonation not only indicates the strong binding affinity that exists between Ca^{2+} and COO^-, but also signals that an excess of Ca^{2+} is present at the interface. With sufficient Ca^{2+}, the 2:1 bridging ionic complex is favored. On the contrary, the D_{31}-PA monolayer is only partially deprotonated on the 0.1 M Ca^{2+} subphase, based on the spectral evidence obtained in the other spectral regions; therefore, even though the 2:1 bridging ionic complex is the dominant species at 0.1 and 0.3 M Ca^{2+}, the 1:1 bidentate ionic complex could well be the secondary channel. This would maximize the overall interaction between a Ca^{2+} ion and the headgroup when Ca^{2+} is limited in quantity at the interface. In conclusion, the interplay between the cation species and the concentration level strongly dictates which stable ionic complexes are formed between the cation and the headgroup.

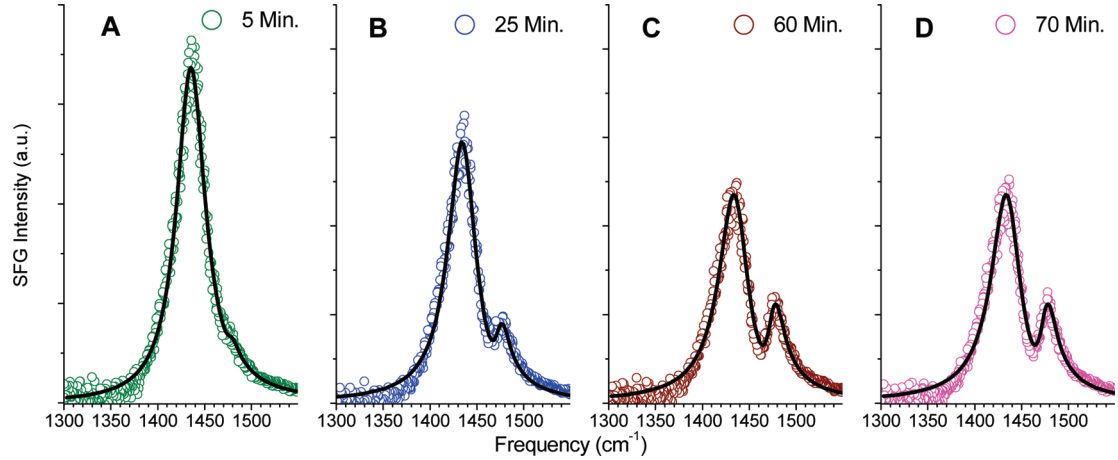

Figure 6. ssp VSFG spectra in the COO^- stretch region of D_{31}-PA monolayers on 0.1 M $CaCl_2$ solutions at near-neutral pH in a time series: (A) 5, (B) 25, (C) 60, and (D) 70 min. The individual fitted curves are shown as solid lines. Each spectrum corresponds to a 5-min acquisition time.

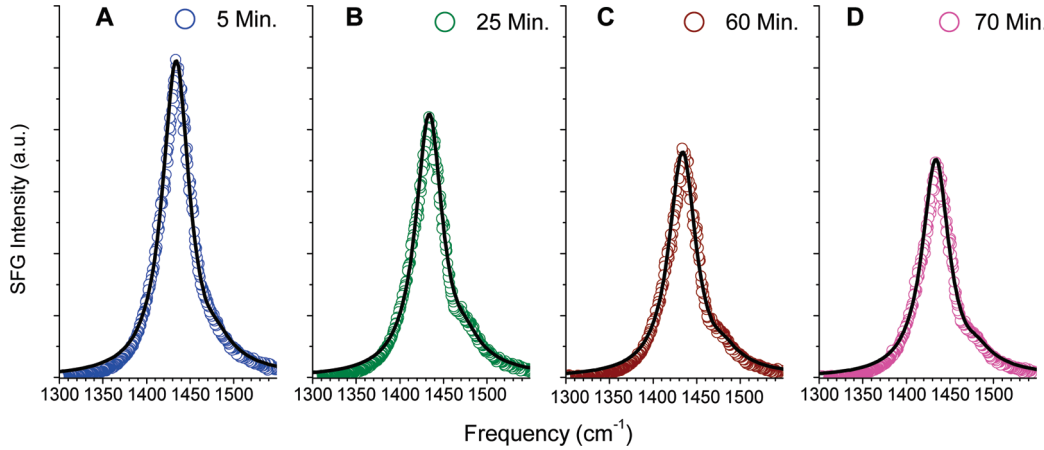

Figure 7. ssp VSFG spectra in the COO^- stretch region of D_{31}-PA monolayers on 0.3 M $CaCl_2$ solutions at near neutral pH in a time series: (A) 5, (B) 25, (C) 60, and (D) 70 min. The individual fitted curves are shown as solid lines. Each spectrum corresponds to a 5-min acquisition time.

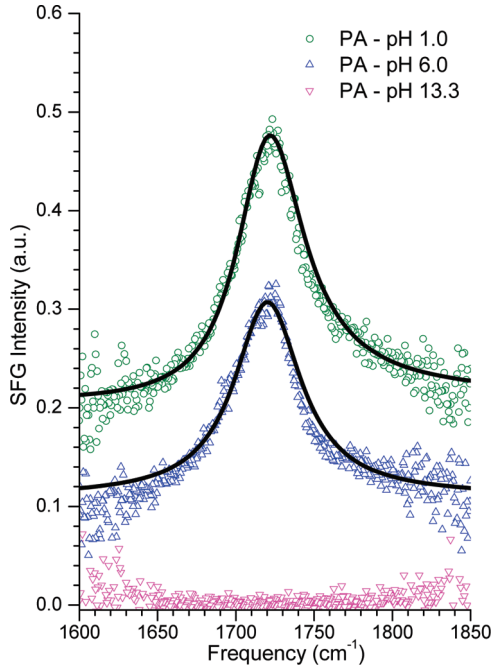

Figure 8. ssp VSFG spectra in the C═O stretch region of PA monolayers on water with pH values of 1.0, 6.0, and 13.3. The fitted curve for pH 1.0 spectrum is shown as a solid line. Spectra are offset for clarity.

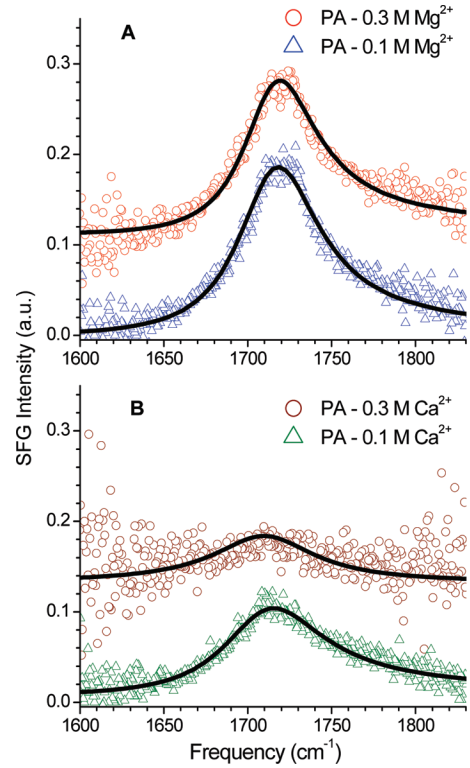

Figure 9. ssp VSFG spectra in the C═O stretch region of PA monolayers on salt solutions at near neutral pH: (A) 0.1 and 0.3 M $MgCl_2$; (B) 0.1 and 0.3 M $CaCl_2$. The individual fitted curves are shown as solid lines. Spectra are offset for clarity.

3.2.3. Carbonyl Stretching (νC═O) Region (1700−1800 cm^{-1}). Because protonated and deprotonated forms of carboxylic acid group have unique vibrational signatures, known as νC═O and $\nu_s COO^-$ modes, respectively, spectral investigations in the νC═O were considered important in confirming the deprotonation events induced by the ionic binding of Mg^{2+} and Ca^{2+} to the PA headgroup. However, to clearly identify the exact spectral position of the νC═O mode, an additional pH control experiment was performed in this spectral region.

3.2.3.1. pH Control Study. Figure 8 shows the ssp VSFG spectra of the PA monolayers on aqueous solutions at pH 1.0, 6.0, and 13.3. At the two extreme pH conditions, PA molecules are either primarily protonated or deprotonated. The νC═O spectra presented in Figure 8 are consistent with the $\nu_s COO^-$ spectra in Figure 3 at the corresponding pH. By observation, at pH 1.0, Figure 8 shows a symmetric peak centered at 1720 cm^{-1}, which is attributed to the hydrated carbonyl group in the carboxylic acid headgroup at this low pH. On the other hand, the same peak becomes hardly detectable at pH 13.3, but only weakens slightly at pH 6.0, consistent with our observations from above.

3.2.3.2. Mg^{2+} vs Ca^{2+}. According to the previous results obtained from the $\nu_s COO^-$, Ca^{2+} demonstrates much stronger ionic binding affinity to the COO^- relative to Mg^{2+}, which then correspondingly induces greater extent of deprotonation on the PA monolayers. To confirm this phenomenon, we again evaluate the spectra with Mg^{2+}(aq) and Ca^{2+}(aq) subphases, but now in the νC═O region. Figure 9A and B show the ssp VSFG spectra of the PA monolayers on Mg^{2+}(aq) solutions and Ca^{2+}(aq) solutions (0.1 and 0.3 M), respectively. The spectra representing the Mg^{2+}(aq) solutions at 0.1 and 0.3 M reveal a broad, slightly asymmetric peak centered at 1720 cm^{-1}. Even though a concentration difference exists in the Mg^{2+}(aq) solutions' spectra, the νC═O peak intensities are almost constant in the

concentration range considered. This observation is in good agreement with the $\nu_s COO^-$ spectral trend seen in the previous section.

The spectra representing the Ca^{2+}(aq) solutions show a significant decrease in the peak intensity when Ca^{2+}(aq) solution is increased from 0.1 to 0.3 M. This is consistent with the observation in the $\nu_s COO^-$. Figure 9B shows significant deprotonation of the PA monolayers on the 0.1 M Ca^{2+} and much more on the 0.3 M. This latter peak intensity becomes almost negligible. Quantitatively, the percent increase in the number of deprotonation is 96% from the 0.1 to 0.3 M Ca^{2+}(aq) solution using the corresponding $\nu C{=}O$ peak intensities (square root); likewise, a similar value (100%) is estimated if based on the $\nu_s COO^-$ data on the same Ca^{2+}(aq) solution. The two spectral regions are in good agreement with respect to an increase in the $\nu_s COO^-$ peak intensity corresponding to a decrease in the $\nu C{=}O$ peak intensity.

4. Conclusions

In this investigation, we reveal the cationic binding specificity of alkaline earth cations Mg^{2+} and Ca^{2+} with the biologically relevant carboxylate ligand from a fatty acid at the air/aqueous interface by directly probing the unbound and bound complexed species. The empirical evidence obtained strongly supports the notion that Ca^{2+} has a stronger binding affinity toward many protein surfaces in biological systems than its counterpart, Mg^{2+}.[3] We conclude that at a near-neutral pH, the mechanism that governs Ca^{2+} binding to COO^- is accompanied by a concomitant deprotonation of the carboxyl acid headgroup. Since the majority of intracellular processes depend on a neutral pH, this may explain why there exists such a considerable Ca^{2+} concentration gradient across the cell membrane.

Surface molecular structure and ion concentration are important factors influencing cation binding behavior at the air/liquid interface, as is shown here. For example, at lower concentration (0.1 M Ca^{2+}), Ca^{2+} initially favors forming ionic complexes in a bridging configuration ($2Ca^{2+}$:$1COO^-$) but a considerable fraction gradually transforms to a chelating bidentate complex ($1Ca^{2+}$:$1COO^-$) as the system reaches equilibrium. On the other hand, as the Ca^{2+} concentration rises to 0.3 M, the primary complexed species exists in the 2:1 bridging configuration, even when sufficient time is given for structural reorganization, as seen in the 0.1 M. This concentration-dependent binding behavior could suggest that Ca^{2+} binding on the protein surface is intrinsically multifold, due to structural complexity at the protein surface, and the binding geometry is controlled by the availability of Ca^{2+} in the aqueous phase.

Acknowledgment. We thank the National Science Foundation, NSF CHE-0749807, for funding this work.

Supporting Information Available: VSFG ssp spectra in the CH stretching region of PA at 30 mN/m on neat water, 0.1 and 0.3 $MgCl_2$ and $CaCl_2$. This information is available free of charge via the Internet at http://pubs.acs.org.

References and Notes

(1) Nies, D. H., Silver, S., Eds.; *Molecular Microbiology of Heavy Metals*; Springer-Verlag: Berlin, 2007; pp 118−227.
(2) Hasebe, N.; Kikuchi, K. Cardiovascular Disease and Magnesium. In *New Perspectives in Magnesium Research: Nutrition and Health*; Nishizawa, Y., Morii, H., Durlach, J., Eds.; Springer-Verlag: London, 2007; pp 227−238.
(3) Vogel, H. J.; Brokx, R. D.; Ouyang, H. Calcium-Binding Proteins. In *Calcium-Binding Protein Protocols*; Vogel, H. J., Ed.; Humana Press, Inc.: Totowa, NJ, 2002; Vol. 1; pp 3−20.
(4) Houston, M. C.; Harper, K. J. *J. Clin. Hypertens.* **2008**, *10*, 3–11.
(5) Dynarowicz-Latka, P.; Dhanabalan, A.; Oliveira, O. N. *Adv. Colloid Interface Sci.* **2001**, *91*, 221–293.
(6) Liu, J.; Conboy, J. C. *J. Am. Chem. Soc.* **2004**, *126*, 8376–8377.
(7) Castellana, E. T.; Cremer, P. S. *Surf. Sci. Rep.* **2006**, *61*, 429–444.
(8) Ma, G.; Allen, H. C. *Langmuir* **2007**, *23*, 589–597.
(9) Liu, J.; Conboy, J. C. *J. Phys. Chem. C* **2007**, *111*, 8988–8999.
(10) Lipp, M. M.; Lee, K. Y. C.; Waring, A.; Zasadzinski, J. A. *Biochem. J.* **1997**, *72*, 2783–2804.
(11) Vacha, R.; Siu, S. W. I.; Petrov, M.; Bockmann, R. A.; Barucha-Kraszewska, J.; Jurkiewicz, P.; Hof, M.; Berkowitz, M. L.; Jungwirth, P. *J. Phys. Chem. A* **2009**, *113*, 7235–7243.
(12) Aston, M. S. *Chem. Soc. Rev.* **1993**, *22*, 67–71.
(13) Mobius, D. *Curr. Opin. Colloid Interface Sci.* **1998**, *3*, 137–142.
(14) McConnell, H. M. *Annu. Rev. Phys. Chem.* **1991**, *42*, 171–195.
(15) Zotti, G.; Vercelli, B.; Berlin, A. *Acc. Chem. Res.* **2008**, *41*, 1098–1109.
(16) Haro, M.; Gascon, I.; Aroca, R.; Lopez, M. C.; Royo, F. M. *J. Colloid Interface Sci.* **2008**, *319*, 277–286.
(17) Kaganer, V. M.; Mohwald, H.; Dutta, P. *Rev. Mod. Phys.* **1999**, *71*, 779–819.
(18) Nylander, T.; Campbell, R. A.; Vandoolaeghe, P.; Cardenas, M.; Linse, P.; Rennie, A. R. *Biointerphases* **2008**, *3*, FB64–FB82.
(19) Klechkovskaya, V.; Anderle, M.; Antolini, R.; Canteri, R.; Feigin, L.; Rakova, E.; Stiopina, N. *Thin Solid Films* **1996**, *284*, 208–210.
(20) Gericke, A.; Huhnerfuss, H. *Thin Solid Films* **1994**, *245*, 74–82.
(21) Simon-Kutscher, J.; Gericke, A.; Huhnerfuss, H. *Langmuir* **1996**, *12*, 1027–1034.
(22) Blaudez, D.; Turlet, J. M.; Dufourcq, J.; Bard, D.; Buffeteau, T.; Desbat, B. *J. Chem. Soc.-Faraday Trans.* **1996**, *92*, 525–530.
(23) Le Calvez, E.; Blaudez, D.; Buffeteau, T.; Desbat, B. *Langmuir* **2001**, *17*, 670–674.
(24) Ren, Y. Z.; Hossain, M. M.; Iimura, K.; Kato, T. *J. Phys. Chem. B* **2001**, *105*, 7723–7729.
(25) Liu, H. J.; Du, X. Z.; Li, Y. *J. Phys. Chem. C* **2007**, *111*, 17025–17031.
(26) Yazdanian, M.; Yu, H.; Zografi, G. *Langmuir* **1990**, *6*, 1093–1098.
(27) Travesset, A.; Vaknin, D. *Europhys. Lett.* **2006**, *74*, 181–187.
(28) Liu, H. J.; Miao, W. G.; Du, X. Z. *Langmuir* **2007**, *23*, 11034–11041.
(29) Kmetko, J.; Datta, A.; Evmenenko, G.; Dutta, P. *J. Phys. Chem. B* **2001**, *105*, 10818–10825.
(30) Malin, J. N.; Hayes, P. L.; Geiger, F. M. *J. Phys. Chem. C* **2009**, *113*, 2041–2052.
(31) Schrodle, S.; Moore, F. G.; Richmond, G. L. *J. Phys. Chem. C* **2007**, *111*, 8050–8059.
(32) Finlayson, A. C. *J. Chem. Educ.* **1992**, *69*, 559–559.
(33) Adamson, A. W.; Gast, A. P. *Physical Chemistry of Surfaces*; Wiley: New York, 1997.
(34) Hommel, E. L.; Allen, H. C. *Anal. Sci.* **2001**, *17*, 137–139.
(35) Ma, G.; Allen, H. C. *J. Phys. Chem. B* **2003**, *107*, 6343–6349.
(36) Tang, C.; Allen, H. *J. Phys. Chem. A* **2009**, *113*, 7383–7393.
(37) Linden, M.; Rosenholm, J. B. *Langmuir* **1995**, *11*, 4499–4504.
(38) Kaganer, V. M.; Peterson, I. R.; Kenn, R. M.; Shih, M. C.; Durbin, M.; Dutta, P. *J. Chem. Phys.* **1995**, *102*, 9412–9422.
(39) Hasegawa, T.; Nishijo, J.; Watanabe, M.; Umemura, J.; Ma, Y. Q.; Sui, G. D.; Huo, Q.; Leblanc, R. M. *Langmuir* **2002**, *18*, 4758–4764.
(40) Shen, Y. R. *The Principles of Nonlinear Optics*; 1st ed.; John Wiley & Sons: New York, 1984.
(41) Deamer, D. W.; Meek, D. W.; Cornwell, D. G. *J. Lipid Res.* **1967**, *8*, 255–263.
(42) Johnson, C. M.; Tyrode, E.; Baldelli, S.; Rutland, M. W.; Leygraf, C. *J. Phys. Chem. B* **2005**, *109*, 321–328.
(43) Miranda, P. B.; Du, Q.; Shen, Y. R. *Chem. Phys. Lett.* **1998**, *286*, 1–8.
(44) Gershevitz, O.; Sukenik, C. N. *J. Am. Chem. Soc.* **2004**, *126*, 482–483.
(45) Gomez-Fernandez, J. C.; Villalain, J. *Chem. Phys. Lipids* **1998**, *96*, 41–52.
(46) Collins, K. D. *Biophys. Chem.* **2006**, *119*, 271–281.
(47) Nakamoto, K. *J. Am. Chem. Soc.* **1957**, 4904.
(48) Curtis, N. F. *J. Chem. Soc. A* **1968**, 1579.
(49) Robinson, S. D.; Uttley, M. F. *J. Chem. Soc., Dalton Trans.* **1973**, 1912–1920.
(50) Deacon, G. B.; Phillips, R. J. *Coord. Chem. Rev.* **1980**, *33*, 227–250.
(51) Nakamoto, K. *Infrared and Raman Spectra of Inorganic and Coordination Compounds*, 4th ed.; Wiley: New York, 1986.
(52) Tackett, J. E. *Appl. Spectrosc.* **1989**, *43*, 483–489.

JP105472E